Tremor-rich shallow dyke formation followed by silent magma flow at Bárðarbunga in Iceland

Eva P. S. Eibl[1*†], Christopher J. Bean[1†], Kristín S. Vogfjörd[2], Yingzi Ying[1†], Ivan Lokmer[1], Martin Möllhoff[1†], Gareth S. O'Brien[3] and Finnur Pálsson[4]

The Bárðarbunga eruption in Iceland in 2014 and 2015 produced about 1.6 km³ of lava. Magma propagated away from Bárðarbunga to a distance of 48 km in the subsurface beneath Vatnajökull glacier, emerging a few kilometres beyond the glacier's northern rim. A puzzling observation is the lack of shallow (<3 km deep), high-frequency earthquakes associated with shallow dyke formation near the subaerial and subglacial eruptive sites, suggesting that near-surface dyke formation is seismically quiet. However, seismic array observations and seismic full wavefield simulations reveal the presence and nature of shallow, pre-eruptive, long-duration seismic tremor activity. Here we use analyses of seismic data to constrain the relationships between seismicity, tremor, dyke propagation and magma flow during the Bárðarbunga eruption. We show that although tremor is usually associated with magma flow in volcanic settings, pre-eruptive tremor at Bárðarbunga was probably caused by swarms of microseismic events during dyke formation, and hence is directly associated with fracturing of the upper 2–3 km of the crust. Subsequent magma flow in the newly formed shallow dyke was seismically silent, with almost a complete absence of seismicity or tremor. Hence, we suggest that the transition from temporarily isolated, large, deep earthquakes to many smaller, shallower, temporally overlapping earthquakes (<magnitude 2) that appear as continuous tremor announces the arrival of a dyke opening in the shallow crust, forming a pathway for silent magma flow to the Earth's surface.

Sustained seismic signals called seismic tremor are often associated with volcanic eruptions, but the exact relationships may vary and are not well constrained. Traditionally, tremor is thought to be directly linked to fluid movement in the subsurface[1]. Tremor models range from boiling-related mechanisms to resonating cracks[2] or pipes[3] to flow-induced excitation and oscillation of the conduit walls[4–6]. More recent tremor models evoke repeating processes such as rock deformation/faulting[7,8] or merging low-frequency events[9] as a possible source of tremor. A common lack of tremor depth estimates and a variety of possible generation processes leave the interpretation of these pre-, syn- and post-eruptive signals open to large uncertainty.

Earthquakes mark dyke propagation at depth

Bárðarbunga volcano in Iceland is one of the most active volcanoes beneath Vatnajökull glacier and its recent activity offers an unique window into seismic tremor generation. From 16 August 2014 a dyke accompanied by 5–8-km-deep earthquakes formed beneath Bárðarbunga volcano, propagating initially in a SE direction. Propagation speeds and directions changed multiple times, with an average direction towards the NNE migrating about 48 km in 11 days (ref. 10). On 29 August 2014 a 4-h-long subaerial eruption started near the tip of the dyke 5 km north of the glacier rim. It stopped only to restart on the same fissure on 31 August 2014, continuing until 27 February 2015[11] and producing 1.6 ± 0.3 km³ of lava[12]. In addition, multiple subglacial eruptions were suspected between 23 August and 5 September (refs 13,14).

The propagation of the growing dyke in the subsurface was well tracked using earthquake locations at 5–8 km depth (Fig. 1). Despite the high levels of seismicity associated with dyke propagation at depth, levels of continuous tremor, often conceptually associated with magma flow, were low. Another remarkable observation is a lack of shallow (<3 km), high-frequency earthquakes during the entire sequence, with most seismicity lying deeper than 5 km even at the eruptive site[10,15]. The exceptional Bárðarbunga eruption was very well instrumented[10,15,16], which allows us to constrain the relationships between seismicity, tremor, dyke propagation and magma flow.

Tremor level during the dyke propagation

We assess the tremor level during dyke propagation and subglacial and subaerial eruptions using the root median square (RMeS) calculated over 14.9 min windows with 80% overlap. This represents the tremor amplitude better than root mean square (RMS) as it filters out discrete earthquakes (Fig. 2b). A closer inspection of Fig. 1 reveals that some tremor pulses seem to temporally correlate with the initiation of dyke propagation. For example, dyke propagation stopped for 81 h from 19 August, and one of the three strongest tremors occurred when it suddenly propagated further northwards on 23 August. A cauldron on the ice surface (C2 in Fig. 1) was observed, a few days later, to have formed above the dyke, suggesting that the dyke may have breached the shallow crust subglacially. However, some tremor pulses do not coincide with the initiation of dyke propagation/faster magma flow (for example, on 20 August). These indicate that the pre-eruptive tremor source is not well correlated with the expected magma flow speed.

The sparse yet intense tremor activity on 23 August was the catalyst for the installation of a 7-station (3-component Güralp 6TDs, 30 s) seismic array at Urdarháls (UR in Fig. 1a) on 30 August. Such arrays are well suited for tremor location[17]. The installation
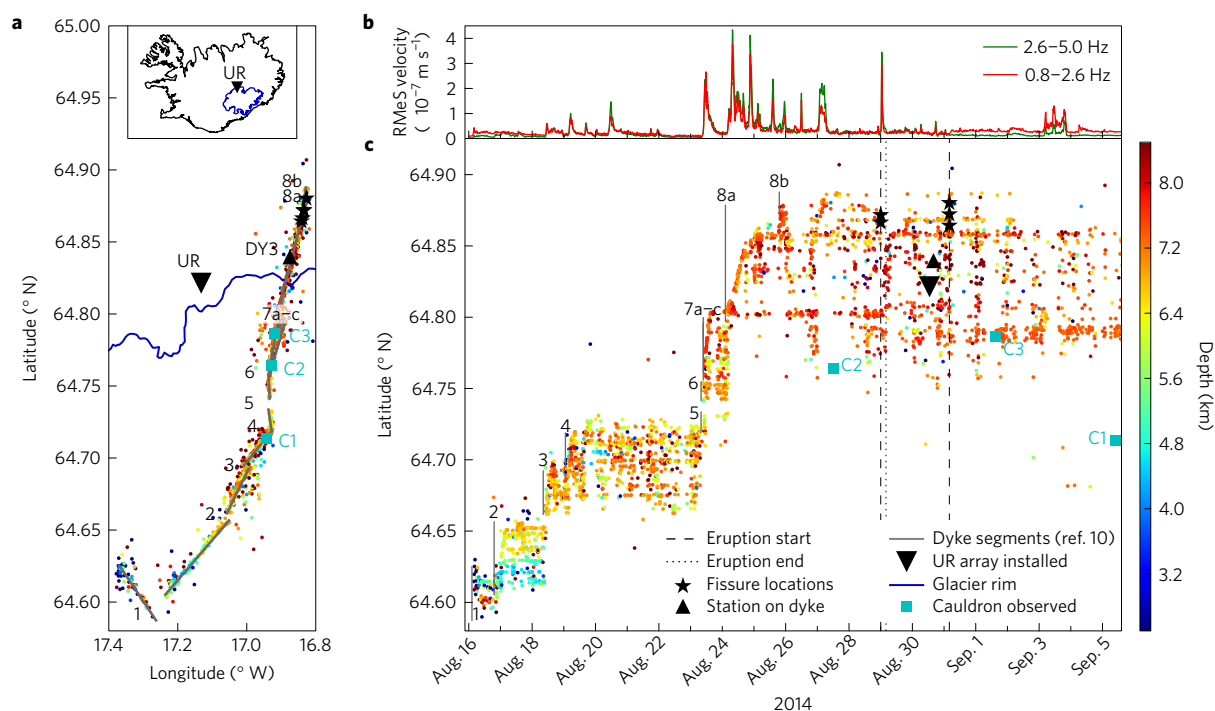
1

Figure 1 | Earthquake locations show the propagation of the dyke at depth. a, Dots indicate relocated earthquakes plotted in latitude and longitude from 16 August until 6 September 2014 coloured according to depth (locations from Fig. 2c (ref. 10)). Grey straight lines indicate dyke segments[10]. Black stars mark the location of the fissures, the black triangle the location of the temporary seismometer DY3 on top of the dyke on August 30th, and the black inverted triangle the installation of the 7-station UR seismic array. Cyan squares C1–C3 mark cauldrons and therefore potential subglacial eruption sites. The inset shows UR and Vatnajökull glacier in Iceland. **b**, The root median square (RMeS) of the seismic data at station KRE from the Icelandic Meteorological Office (IMO) network (see Fig. 3 for the location) is shown filtered between 0.8 and 2.6 Hz and between 2.6 and 5.0 Hz. **c**, Dots, grey lines, black stars, black triangle and black inverted triangle as in **a**. Dashed and dotted vertical lines mark the start and end of a subaerial eruption, respectively. C1–C3 mark when cauldrons were first observed during flights, or identified in aerial photos, although they might have formed earlier (Hannah I. Reynolds & Magnús T. Gudmundsson, personal communication, Feb. 2016).

was completed between the 4-h-long subaerial fissure eruption of 29 August and the 6-month-long subaerial eruption from 31 August (Fig. 1c). UR is 12 km from the fissure and gives us the opportunity to analyse the tremor in detail. We can see an increase in tremor, especially around 1 Hz after 31 August, which marks the beginning of the subaerial eruption and the beginning of syn-eruptive tremor. The back azimuth obtained from the array clearly points towards the eruptive site whilst no concurrent tremor was detected along the 48-km-long eruption-feeding dyke. However, we focus in the remainder of this study on the anomalously high pre-eruptive tremor with a different back azimuth on 3 September. We refer to it as pre-eruptive as it marks the site where a local, subglacial eruption was suspected based on cauldron formation between 23 August and 5 September (refs 13,14). It is approximately 12 km south of the main ongoing subaerial eruption. Array analysis of this tremor is undertaken to understand its precise causative mechanism.

Shallowing of the pre-eruptive tremor source

The tremor on 3 September started emergently around midnight and ended abruptly at 21:35 (Fig. 2). By 2:00 it was stronger than the syn-eruptive tremor from the ongoing subaerial eruption and had maximum amplitudes from 10:30 to 12:30 and from 18:30 to 20:30. The tremor was harmonic, with a first faintly visible frequency band at 0.55 Hz and overtones at a spacing of approximately 0.25 Hz (Fig. 2d). During the whole tremor sequence most energy was concentrated around 1.3 Hz. Whilst the tremor amplitude changed only slightly during the first 5.5 h it waxed and waned, still retaining its harmonic character from 9:00 and especially from 19:38 tremor entered a start–stop phase still showing harmonic frequency bands when present. It first stopped for 1.5 min at 15:49:29, then for

1.3 min at 17:16:59, and much more often from 19:38, when the longest gap was 10.3 min and the shortest about 7 s.

Temporal changes are also visible in the back azimuth and slowness at UR array (see Methods, ref. 18 and Fig. 2a). The tremor back azimuth initially stabilized around 122°. From 3:30 it decreased to 119° and moved from there in steps to 128, 123 and 134°. Between the steps the back azimuth stabilized for time periods of up to 6 h. Slownesses increased from 0.57 to 0.75 s km^{-1} and correlated with the steps in back azimuth. Hence, we can determine that the tremor source shallowed and moved overall southwards in pulses over a 19 h period.

The back projection along the estimated back azimuth (Fig. 3b) indicates that the tremor came from a region southeast of UR. We constrain the location horizontally by applying an amplitude location method (see Methods and refs 19,20) using permanent stations in the area (triangles in Fig. 3b). The horizontal locations are spread in a NNE–SSW direction which is consistent with the elongation of the location error ellipse in that direction (not shown). We determine that the epicentre of the tremor is laterally consistent with the dyke location (as defined by relatively relocated earthquakes at 5–8 km depth[10]) and cauldron C1 to C3 locations. In this instance the tremor depth is not constrained by array analysis but is determined in the next section with the aid of full waveform numerical simulations (see Supplementary Fig. 2e for a location precision test using a well-located earthquake).

Tremor models and tremor simulations

On closer inspection of the tremor there are seven important observations: we find evidence of discrete events in the tremor that come from the same location as the tremor itself (marked with red arrows
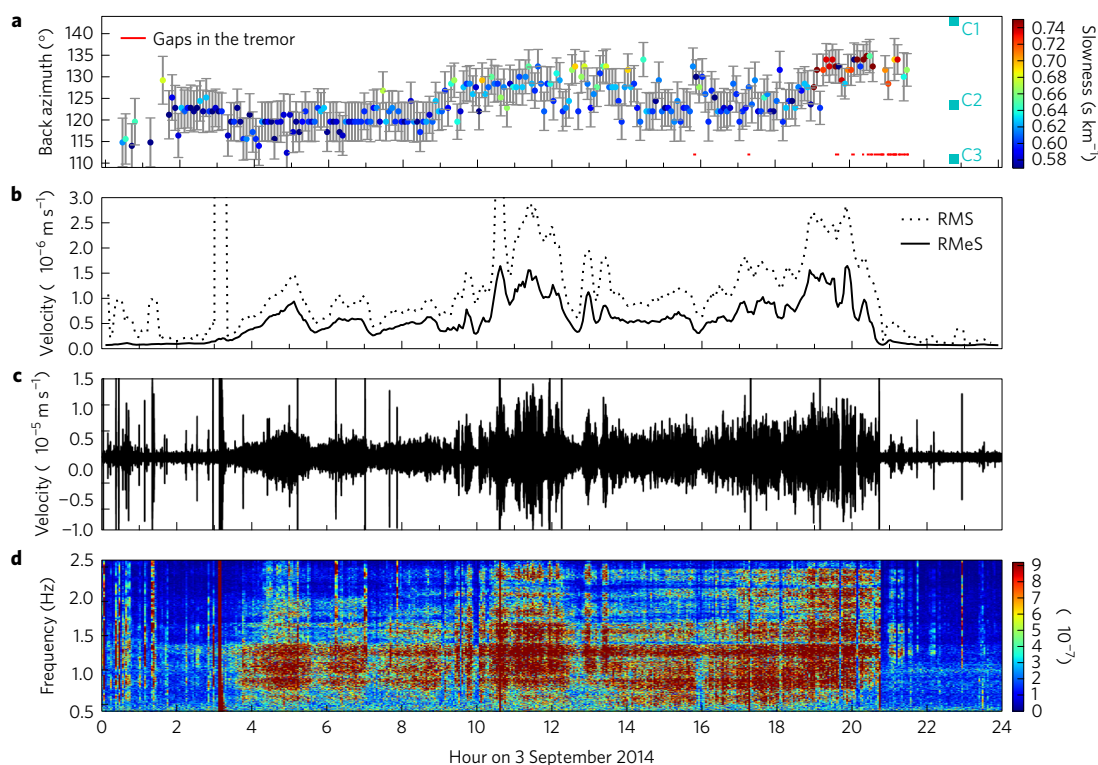
Figure 2 | Laterally moving and shallowing pre-eruptive tremor on 3 September 2014. a, Dots indicate the back azimuth coloured according to horizontal slowness. The red horizontal lines indicate times when the tremor stopped completely and cyan squares mark the back azimuth of cauldrons C1–C3. **b**, RMS and RMeS averaged over the vertical component of all seven stations in the UR array. **c**, Instrument-corrected seismogram of the vertical component at station URA of UR array filtered between 0.4 and 2.6 Hz. **d**, Amplitude spectrogram of **c** with a fast Fourier transform window length of 256 s.
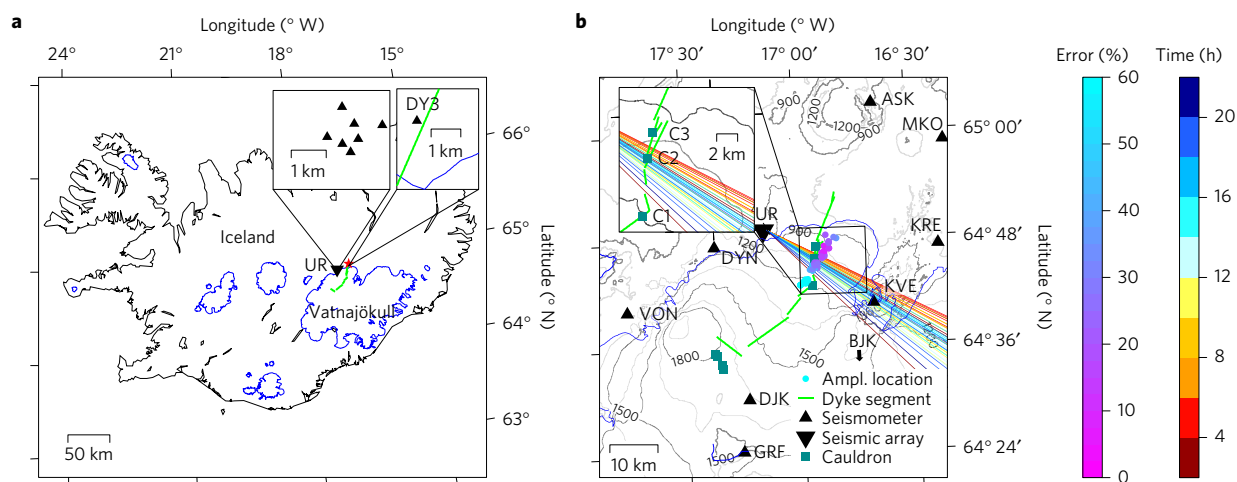

Figure 3 | Projected back azimuth and amplitude location of the pre-eruptive tremor. a, Location of UR in Iceland with respect to glaciers, the dyke (green lines) and the subaerial eruption site (red star). The insets show the geometry of UR and location of DY3 on 30 August. **b**, Amplitude (Ampl.) location estimates of the tremor on 3 September 2014 are shown in the 3–4 Hz band. Lines indicate the mean back azimuth in each half hour coloured according to time. Dots indicate the best fit gridpoint in the amplitude distribution in each time window, coloured according to the minimum location error percentage. Site corrections as in Supplementary Table 1 were applied. Elevation in metres above sea level based on data from the National Land Survey of Iceland. The inset shows the location of the cauldrons with respect to the back azimuth, in more detail.

in Fig. 4a); temporal gaps indicate an erratic tremor generating process; there is a lack of sustained tremor from the dyke accompanying the persistent constant lava flow from the subaerial eruptive fissure after 31 August; tremor is in some cases temporarily correlated with pulsations in dyke propagation; the fastest dyke propagation (4.7 km h^{-1}) on 23 August (ref. 15) does not coincide with the highest tremor amplitude (24 August) and further propagation speeds above 4.0 km h^{-1} on 16 and 18 August (ref. 15) occur at times of very low tremor amplitudes; on 3 September the tremor source moves

at least 3.1 km horizontally in 19 h; and the tremor source moves upwards (shallows) with a prominent jump around 19:00.

As possible tremor-generation processes here we consider fast flow of magma, repeating earthquakes and boiling activity. The boiling temperature of water at 2 km depth is about 350 and 441 °C under hydrostatic and lithostatic pressure conditions, respectively[21]. These temperatures are achievable given a temperature of more than 1,100 °C for the effusing lava[22]. However, for hydrothermal boiling we would expect that an increase in available water
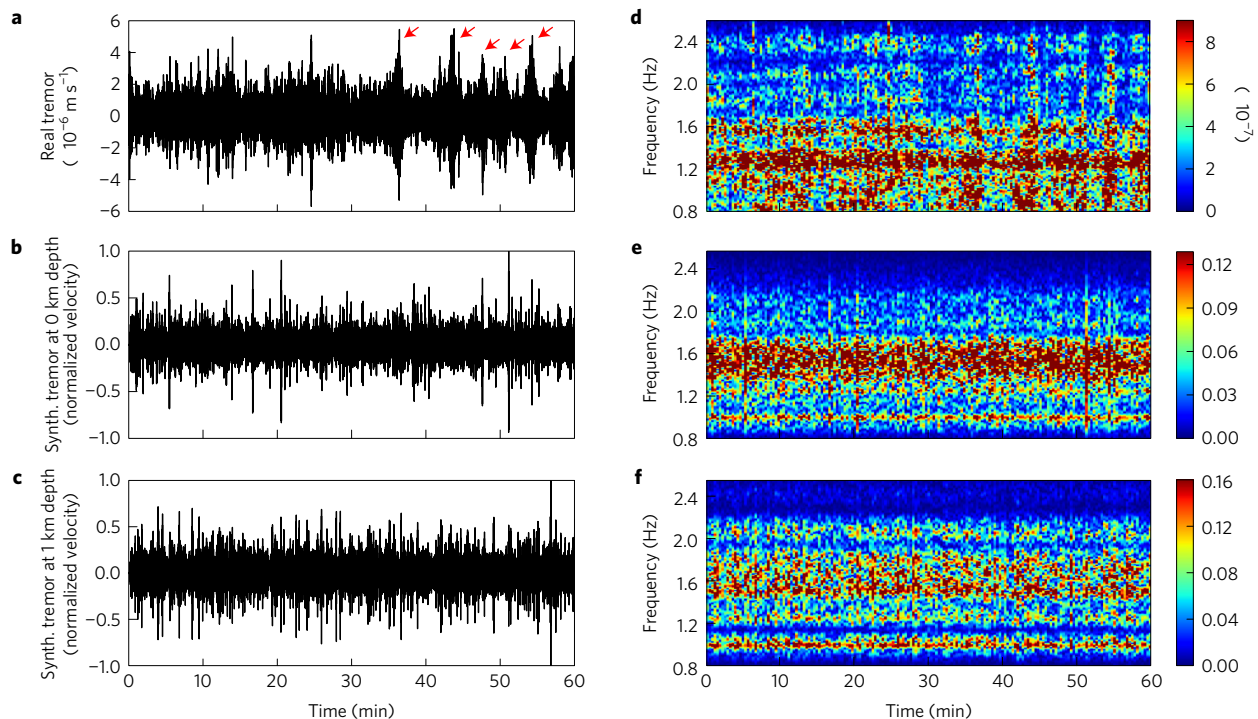
Figure 4 | Comparison of real and synthetic tremor. Synthetic tremor simulated by the convolution of a synthetic microseismic (Ricker wavelet) event beneath C2 recorded at UR array with a quasi-comb function with a 4 s mean time spacing, 7% time spacing variation and an amplitude distribution derived from the real tremor. **a**, Horizontal velocity seismogram of real field tremor between 14:00 and 15:00 where slownesses in Fig. 2a indicate that the tremor source is at 1 km depth at that time. **b**, Same as **a** but for synthetic tremor from a source at 0 km depth. **c**, Same as **b** but for a source at 1 km depth, **d**, Real field tremor amplitude spectrogram. **e**, Amplitude spectrogram of the synthetic tremor from a source at 0 km depth. **f**, Same as **e** but for a source at 1 km depth. All spectrograms are made with a fast Fourier transform window length of 32 s. Red arrows mark individual events in the real tremor, that are colocated with the tremor source.

and decrease in pressure (upwards movement) would lead to an increase in observed tremor amplitude. Instead, with upward tremor migration the tremor amplitude dies down while gaps in the tremor become prominent.

We investigated the possibility of magma-flow-induced tremor generation using Julian's[4] established fluid-flow-driven nonlinear conduit excitation model. Model parameters were constrained by field measurements[10,22] (see Methods). The model was run using all possible combinations of these parameters. We found that for most combinations the system exhibits steady state behaviour without generating tremor. If present in the model, tremor frequencies are below 0.005 Hz for the field parameters used here, almost two orders of magnitude smaller than observed tremor frequencies. This is in accordance with Balmforth[23], who found that magma-induced tremor from instability requires very narrow cracks and high flow velocities; conditions that are unlikely to be satisfied in general. Similar results on tremor generation were obtained from tests in the laboratory[6] and theoretical analysis[5]. In general, tremor could be generated in these models, but only if the flow speed was high enough or the dimensions of the resonating body were adapted to fit the observed tremor frequencies. However, putting it in geological context, these models required either unrealistically high flow speeds or physical dimensions, for example for the resonating body, that were unrealistically large[6]. Consequently, for example, Hellweg[5] concluded that if one of their models applies, then tremor was generated by the movement of water or gases and not by magma. Based on our above calculations and observations we explore a model of repeating microearthquake sources rather than flowing magma or hydrothermal boiling as an explanation for the observed tremor.

To investigate this model, synthetic tremor is generated with the aid of full wavefield numerical simulations in a realistic topographic and velocity model[24]. Our velocity model is based on a published

velocity model in the volcanic zone around Vatnajökull glacier[25] and small-scale refraction seismic studies on volcanoes[26,27] (see Fig. 5a and Methods). We calculate full wavefield synthetic seismograms at all UR station locations for Ricker wavelet sources at 0, 0.5, 1, 3 (see Supplementary Fig. 3), 5, 7 and 10 km depth beneath cauldron C2, based on the field tremor epicentral location obtained from the amplitude and array analysis (Fig. 3). Depth values are with respect to the bedrock–ice interface. These synthetic seismograms are then convolved with a quasi-comb function with a mean spike spacing of 4 s in order to simulate tremor, as detailed in the Methods. As the mean spacing of the spikes in the comb is small in comparison to the duration of each single recorded synthetic event at UR's location, body and surface waves overlap, producing a continuous tremor wavefield. Synthetic and real tremor can be compared in Fig. 4 and Supplementary Fig. 4. Despite the sensitivity to the comb details and the wavelet, our synthetic waveforms and spectrograms are reasonably similar to observed tremor.

The resulting synthetic tremor was then analysed using array processing to constrain the depth of the real tremor based on slowness estimates. With decreasing source depth, median slownesses increase towards surface wave slownesses (Fig. 5b) as observed in reality (see Fig. 2a). The maximum depth of the tremor source is the one which corresponds to the lowest observed slowness (Fig. 5b). The simulations suggest that from 2:00 to 21:35 on 3 September the tremor source moved from 1.8 ± 0.3 km depth to less than 0.5 ± 0.4 km depth. This is supported by the observation that the final tremor slownesses are 0.75 s km^{-1}, which is in the range of typical surface wave slownesses in Iceland and suggests a strong surface wave component. That the character of the tremor changed following the final upward movement (see Fig. 2d) supports a change in environment such as reaching the bedrock surface (beneath the ice). This is also consistent with our hypothesis that
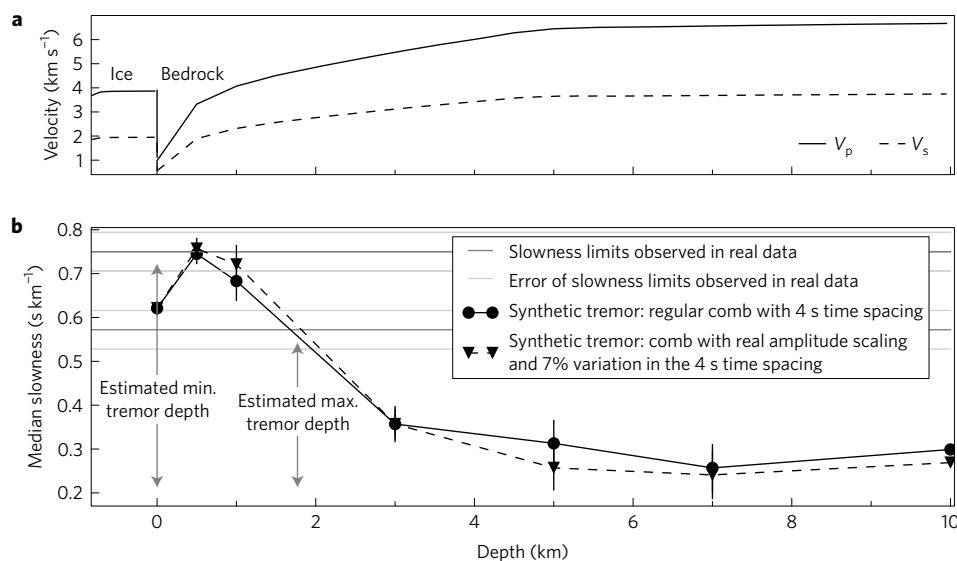
Figure 5 | Tremor simulations indicate a tremor source depth of less than 2 km. a, Velocity model for P and S waves in bedrock and ice in the volcanic zone around Vatnajökull (see Methods). **b**, Median slownesses observed for synthetic tremor created with sources at different depths beneath cauldron C2. Grey horizontal lines mark the minimum and maximum slowness from array analysis of the tremor at UR array on 3 September 2014. Light grey lines and black vertical lines mark the associated error in the slownesses (for details on the error estimation see Methods).

the tremor consists of closely spaced microseismicity and with a deepening of cauldron C2 on the ice surface that was observed on 5 September (ref. 13).

Tremor marks shallow dyke formation

A picture is emerging in which pre-eruptive tremor is associated with shallow dyke propagation but does not appear to be directly related to magma flow. Once the subaerial fissure opened no tremor is detected along the dyke feeding it. This observation is further supported by a short-term deployment directly on an already formed surface fracture zone directly on/above the dyke (station DY3 (ref. 16), black triangle in Figs 1, 3a and Supplementary Fig. 5). No tremor is evident.

Here we propose the following: first, the propagation of dykes at depth (> about 3 km) can be well constrained by seismicity rather than by tremor. Second, shallow dyke formation (<3 km depth) occurs in a region with a lack of high-frequency earthquakes but is instead accompanied by pre-eruptive tremor. Third, pre-eruptive tremor is created by repeating microearthquakes that initiate when rock is fractured in shallow (< about 3 km) dyke formation—probably at dyke tips ahead of the arrival of 'first magma' in the dyke. Fourth, magma flows silently or might be accompanied by weak tremor below the detection threshold of normal instrumentation (at about 12 km distance in our case) in already formed dyke pathways. Fifth, a drop in high-frequency seismicity and onset of tremor can announce the arrival of a dyke-forming magma pathway in the uppermost few kilometres of the crust shortly before an eruption. We hypothesize that the uppermost crust in the volcanic rift zone is too weak to sustain regular high-frequency earthquakes, but instead breaks through swarms of microseismic events, closely spaced in time, and hence appears as continuous tremor at seismic stations. Last, for shallow dyke formations, tremor can be used to deduce shallow (<3 km) dyke emplacement rates. We deduce an average dyke propagation rate of $0.22 \, \text{km} \, \text{h}^{-1}$ from 16 h of lengthening—1.8 km vertically and 3.1 km horizontally. Our rates are slightly lower than the rates observed elsewhere[15,28–30] and are non-steady state.

These interpretations find further support in the following three observations: first, most dyke-related seismicity was in the 5 to 8 km depth range according to results from the IMO permanent network[10] and a temporary, more dense network[15]. However,

shallowing seismicity at less than 5 km depth was observed around C1 and C2 before 27 August (Fig. 1 and ref. 15). Second, we observed that jumps in tremor back azimuth coincide with increases in tremor amplitude (see Fig. 2a), including up to magnitude 2 events within the tremor (Supplementary Fig. 6). Third, that observations that magma can flow silently[31], slowly changing flows can be aseismic[32] and only channels with strong barriers cause tremor[31] were found in earlier tremor studies.

Here we propose that pre-eruptive tremor is a marker for brittle failure in the weak upper 2–3 km of the crust and is therefore intimately related to near-surface dyke formation. In this scenario seismicity tells us about magma flow pathways at depth, whilst the transition to tremor indicates breakthrough to the uppermost crust. At Bárðarbunga, once upper crustal dykes were formed they no longer produced tremor and $1.6 \pm 0.3 \, \text{km}^3$ of magma[12] flowed silently through the uppermost crust to eruption. As the Bárðarbunga eruption was an exceptionally well instrumented type-example of crustal growth with weak if any tremor along the magma feeding dyke, our observations help advance the interpretation of pre-eruptive tremor signals in rifting environments in general.

Methods

Methods, including statements of data availability and any associated accession codes and references, are available in the online version of this paper.

References

1. McNutt, S. R. Volcanic tremor wags on. *Nature* **470**, 471–472 (2011).
2. Chouet, B. A. Dynamics of a fluid-driven crack in three dimensions by the finite difference method. *J. Geophys. Res.* **91**, 13967 (1986).
3. Chouet, B. Excitation of a buried magmatic pipe: a seismic source model for volcanic tremor. *J. Geophys. Res.* **90**, 1881–1893 (1985).
4. Julian, B. R. Volcanic tremor: nonlinear excitation by fluid flow. *J. Geophys. Res.* **99**, 11859–11877 (1994).
5. Hellweg, M. Physical models for the source of Lascar's harmonic tremor. *J. Volcanol. Geotherm. Res.* **101**, 183–198 (2000).
6. Rust, A. C., Balmforth, N. J. & Mandre, S. The feasibility of generating low-frequency volcano seismicity by flow through a deformable channel. *Geol. Soc. Lond.* **307**, 45–56 (2008).

7. Powell, T. W. & Neuberg, J. Time dependent features in tremor spectra. *J. Volcanol. Geotherm. Res.* **128,** 177–185 (2003).
8. Hotovec, A. J., Prejean, S. G., Vidale, J. E. & Gomberg, J. Strongly gliding harmonic tremor during the 2009 eruption of Redoubt Volcano. *J. Volcanol. Geotherm. Res.* **259,** 89–99 (2013).
9. Chouet, B. A. Long-period volcano seismicity: its source and use in eruption forecasting. *Nature* **380,** 309–316 (1996).
10. Sigmundsson, F. *et al*. Segmented lateral dyke growth in a rifting event at Barðarbunga volcanic system, Iceland. *Nature* **517,** 191–195 (2015).
11. Hjartardóttir, Á. R., Einarsson, P., Gudmundsson, M. T. & Högnadóttir, T. Fracture movements and graben subsidence during the 2014 Bárðarbunga dike intrusion in Iceland. *J. Volcanol. Geotherm. Res.* **310,** 242–252 (2015).
12. Gíslason, S. *et al*. Environmental pressure from the 2014–15 eruption of Bárðarbunga volcano, Iceland. *Geochem. Perspect. Lett.* **1,** 84–93 (2015).
13. Scientific Advisory Board of the Icelandic Civil Protection. *Factsheet-Bárðarbunga-20140906* (Icelandic Met Office, 2014); http://en.vedur.is/media/jar/Factsheet-Bardarbunga-140906.pdf
14. Pfeffer, M. A. *et al*. *Factsheet-Bárðarbunga-20140823* (Icelandic Met Office, 2014); http://en.vedur.is/media/jar/Bardarbunga_Daily_status _report_230814.pdf
15. Ágústsdóttir, T. *et al*. Strike-slip faulting during the 2014 Bárðarbunga-Holuhraun dike intrusion, central Iceland. *Geophys. Res. Lett.* **43,** 1495–1503 (2016).
16. Thun, J. *et al*. Micrometre-scale deformation observations reveal fundamental controls on geological rifting. *Sci. Rep.* **6,** 36676 (2016).
17. Almendros, J., Abella, R., Mora, M. M. & Lesage, P. Array analysis of the seismic wavefield of long-period events and volcanic tremor at Arenal volcano, Costa Rica. *J. Geophys. Res.* **119,** 5536–5559 (2014).
18. Capon, J. High-resolution frequency-wavenumber spectrum analysis. *Proc. IEEE* **57,** 1408–1418 (1969).
19. Taisne, B., Brenguier, F., Shapiro, N. M. & Ferrazzini, V. Imaging the dynamics of magma propagation using radiated seismic intensity. *Geophys. Res. Lett.* **38,** L04304 (2011).
20. Eibl, E. P. S., Bean, C. J., Vogfjörd, K. & Braiden, A. Persistent shallow background microseismicity on Hekla volcano, Iceland: A potential monitoring tool. *J. Volcanol. Geotherm. Res.* **289,** 224–237 (2014).
21. Doering, E., Schedwill, H. & Dehli, M. *Grundlagen der Technischen Thermodynamik* (Springer, 2008).
22. Gudmundsson, M. T. *et al*. Gradual caldera collapse at Bárðarbunga volcano, Iceland, regulated by lateral magma outflow. *Science* **353,** aaf8988 (2016).
23. Balmforth, N. J., Craster, R. V. & Rust, A. C. Instability in flow through elastic conduits and volcanic tremor. *J. Fluid Mech.* **527,** 353–377 (2005).
24. Björnsson, H. & Einarsson, P. Volcanoes beneath Vatnajökull, Iceland: evidence from radio echo-sounding, earthquakes and jökulhlaups. *Jökull* **40,** 147–168 (1990).
25. Flóvenz, Ó. G. & Gunnarsson, K. Seismic crustal structure in Iceland and surrounding area. *Tectonophysics* **189,** 1–17 (1991).
26. Ferrazzini, V., Aki, K. & Chouet, B. Characteristics of seismic waves composing Hawaiian volcanic tremor and gas-piston events observed by a near-source array. *J. Geophys. Res.* **96,** 6199 (1991).
27. DeLuca, G., Scarpa, R., Del Pezzo, E. & Simini, M. Shallow structure of Mt Vesuvius volcano, Italy, from seismic array analysis. *Geophys. Res. Lett.* **24,** 481–484 (1997).
28. Einarsson, P. & Brandsdóttir, B. Seismological evidence for lateral magma intrusion during the July 1978 deflation of the Krafla Volcano in NE-Iceland. *J. Geophys.* **47,** 160–165 (1980).
29. Belachew, M. *et al*. Comparison of dike intrusions in an incipient seafloor-spreading segment in Afar, Ethiopia: seismicity perspectives. *J. Geophys. Res.* **116,** 2156–2202 (2011).
30. Buck, W. R., Einarsson, P. & Brandsdóttir, B. Tectonic stress and magma chamber size as controls on dike propagation: constraints from the 1975-1984 Krafla rifting episode. *J. Geophys. Res.* **111,** B12404 (2006).
31. Aki, K. & Koyanagi, R. Deep volcanic tremor and magma ascent mechanism under Kilauea, Hawaii. *J. Geophys. Res.* **86,** 7095–7109 (1981).
32. Ferrick, M. G., Qamar, A. & Lawrence, W. F. S. Source mechanicm of volcanic tremor. *J. Geophys. Res.* **87,** 8675–8683 (1982).

Author contributions

E.P.S.E., C.J.B. and M.M. participated in instrument installation and data collection from seismometers in Iceland and analysing the data. E.P.S.E carried out processing including amplitude locations, array locations and tremor simulations. K.S.V. relocated earthquakes in the dyke and participated with E.P.S.E., C.J.B. and I.L. in the interpretation of the results. Numerical wavefield simulations were performed by Y.Y. on the basis of the topography provided by F.P. G.S.O'B. performed tremor simulations due to magma flow. All authors contributed to the preparation of the manuscript.

Additional information

Supplementary information is available in the online version of the paper. Reprints and permissions information is available online at www.nature.com/reprints. Correspondence and requests for materials should be addressed to E.P.S.E.

Competing financial interests

The authors declare no competing financial interests.

Methods

Frequency wavenumber analysis. As tremor has no clear P and S wave arrivals, traditional travel time location methods cannot be used to locate tremor sources. In contrast, clusters of stations can be used to determine the back azimuth (the direction from which tremor waves are coming). Two or more such arrays allow a determination of the epi-central location of the source.

For the joint determination of back azimuth and slowness of a wave, both frequency domain methods[18,33,34] and time domain methods exist[35–37] and were compared[17,38]. We perform a frequency wavenumber (FK) analysis with a moving time window[18]. The FK analysis is a beamforming method in the spectral domain that performs a grid search within a horizontal slowness grid (s_x and s_y)[39,40]. In each time window the covariances of the Fourier transformed signal at each receiver pair are calculated. Phase delays of each plane wave described by the horizontal slowness grid are applied and the trace of the resulting covariance matrix is the cross spectral density. This is undertaken for every grid point and results in absolute power and semblance maps (ratio of the averaged power of the stacked trace and the stack of the average single trace powers) in the spectral domain with respect to the horizontal slownesses. The maximum value in these maps is determined and converted to back azimuth and slowness of the incoming wave using the angle and length of the vector from the origin to the maximum, respectively. The underlying assumptions include a plane wavefront, coherent signal and incoherent noise.

Based on the array response function of our array we chose a horizontal slowness grid with a limit of $\pm 0.6\,\text{s}\,\text{km}^{-1}$ and a stepsize which is one quarter the width of the main lobe at its half height. The stepsize depends on the number of stations and is, for our seven stations, a minimum of $0.02\,\text{s}\,\text{km}^{-1}$. We remove trend, taper, instrument correct, filter between 0.8 and 2.6 Hz and decimate the vertical component of the data to a sampling frequency of 20 Hz. The recordings from all available stations in the array are then used in the array processing.

To process tremor the whole data set is divided into one-hour-long time windows. For the array processing the time window is subdivided into 30% overlapping time windows that were 10 dominant periods long (5.88 s). In each of these windows the standard FK analysis[18] is performed. The result is a time series of back azimuth, horizontal slowness, semblance and absolute power of the predominant signal in each time window. Changes in the back azimuths suggest a source movement, while a change in slowness reveals different phases arriving at the array (due to the source movement or the change in the wavefield character). We assess the dominant back azimuth with histograms with 0.8°-wide bins and pick the maximum. One standard deviation of the back azimuth during 3 September is between 4 and 10°, depending on the signal-to-noise ratio. We derive the dominant slowness by calculating the median of the continuous tremor slowness. We require a lower limit for the semblance of 0.3 based on the characteristics of our data.

The error in back azimuth and slowness is determined by calculating back azimuth and slowness for each point in the grid at which the power is above 95% of the maximum[41]. The standard deviation of the back azimuths and slownesses of all these points is shown as the error and is in the range of 3.5 to 5.5°. The errors associated with array analysis are linked among other things to the array geometry, including array aperture, number of stations and interstation distances. The signal-to-noise ratio and noise level affect the coherency of the waveforms, and therefore the error. Propagation factors such as the ray paths or reflections can also decrease the coherence across the array[42]. The time sampling, grid search and binning for the histograms induces further errors[41].

Amplitude location method. We use ten stations from the IMO network around northwestern Vatnajökull to perform an amplitude-based location method of the tremor. We subdivided the tremor into 30-minute-long time windows and detrended, instrument corrected, filtered and calculated the RMS of the seismograms. Since the amplitude location methods assume an isotropic radiation pattern from the source, it is desirable to perform the analysis at frequencies above 5 Hz where the path effect has scattered the waves, resulting in an isotropic radiation pattern[43]. But since the signal strength strongly decreases above 2.6 Hz with only little energy remaining from 2.6 to 5 Hz we chose to filter the data between 3 and 4 Hz. We perform a grid search in three dimensions assuming propagating body waves and fit the amplitudes[19] according to:

$$\frac{I_i(r_i)}{I_j(r_j)} = e^{\frac{\pi f}{Q\beta}(r_j - r_i)}\left(\frac{r_j}{r_i}\right) \qquad (1)$$

I_i and I_j are the signal amplitudes at station i and j, r_i and r_j are the distance between the source and seismometer i and j, f is the dominant frequency of the signal, Q is the quality factor for attenuation and β is the S wave velocity in m/s. Performing the location assuming surface waves did not change the tremor location.

Further details of the method and tests performed with the amplitude-based location method can be found in other studies[20,44]. It is shown that the method works well for events inside the network, especially above 4 Hz, and is only slightly affected by the chosen quality factor and velocities[20].

We did not manage to find enough usable teleseismic events within the analysed time period to calculate site correction factors using teleseismic coda due to a high

level of seismicity from Bárðarbunga volcano and the dyke formation. Regional events could not be included due to a station spacing of 10 to 80 km. To estimate site correction factors we used locations of well-constrained events beneath the cauldrons and in the dyke. Root mean square (RMS) amplitudes at the stations were estimated, normalized and plotted against the hypocentral distance from the station location. The amplitude distribution was then fitted with an exponentially decaying curve assuming body wave decay as shown in Supplementary Fig. 1. For the curve fit amplitudes from station KVE were discarded as they were too high for all events from the dyke region. This station was not excluded from the amplitude locations but has a very high site correction factor. Site correction factors for each station were then calculated by dividing the observed amplitudes by the amplitude expected from the curve fit averaged over all events.

Fitting the curve also gives an estimate for $(\pi f)/(Q\beta)$. As f and π are known it is possible to estimate $Q\beta$. Derived site correction factors from the best fitting curve in Supplementary Fig. 1 and $Q\beta$ are shown in Supplementary Table 1.

Total wavefield simulations. We used a glacier surface and bedrock topography model in the western Vatnajökull region based on high-resolution airborne LiDAR surveys or optical satellite images and radio-echo sounding profile on the glacier[45], respectively, to estimate the seismic path effects caused by the glacier. The models have a resolution of 50 m and 500 m, respectively. We used them to build a model of western Vatnajökull and run three-dimensional full wavefield elastic simulations in SPECFEM3D[46] that encompasses seven array stations and nine IMO stations. We implemented the velocity model and densities as described below. 1 Hz Ricker wavelets are used as synthetic seismic sources. We assume observed double couple mechanisms[10] and modelled the total seismic wavefield at 16 synthetic seismometer locations in the model.

Velocity model. We studied published velocity models of the upper and lower crust in the volcanic zone around Vatnajökull glacier, Iceland. We excluded velocity models of the whole island or in regions of central volcanoes and tertiary rocks. The remaining models include two Askja velocity models of refs 47,48 and the velocities on the southern end of the ref. 49 velocity model. We also included the velocity model calculated in ref. 25, who reinterpreted the refraction profiles of ref. 50 with a gradually increasing velocity gradient. The above-mentioned velocity models are consistent in depth, but P wave velocities near the surface range from 2 to 4 km s^{-1}. We expect this as the near-surface velocity structure is poorly constrained by regional-scale refraction seismic experiments. We therefore studied the real slownesses of well-located earthquakes. We simulated these slownesses in various velocity models and found that the model of ref. 25 fits the best. But due to a station spacing of 1 to 4 km (ref. 50) the top few hundred metres are not well resolved, which we constrained with small-scale refraction studies on other volcanoes[26,27]. We lowered the velocities in the first 200 m of the model of ref. 25 and created the velocity model shown in Fig. 5a. A 0 km depth corresponds to the elevation of the bedrock–ice interface. We calculate v_s based on a Poisson ratio of 0.26 in the upper crust and 0.27 in the lower crust (refs 50,51) and the density ρ according to ref. 52.

Ice properties. Temperature profiles in the temperate Vatnajökull glacier measured 0 °C at the surface, and -0.9 °C at 1 km depth (Thorsteinn Thorsteinnsson, Tómas Jóhannesson, personal communication, Feb. 2015). Various studies[53–55] found that the P wave velocity in 0 °C cold ice increases from 3.5 km s^{-1} at 100 m to 3.8 or 3.9 km s^{-1} at 600 m depth. This is consistent with values of 3.6 km s^{-1} measured at Grimsvötn volcano[56,57]. We use the increase of v_p with depth as published in ref. 54 as an approximation and calculate v_s based on a Poisson ratio of 0.33 (refs 53,55). Densities of 0.5 g cm^{-3} were measured at the surface and 0.9 g cm^{-3} at 40 m depth at 1790 m elevation at Hofsjökull glacier (Thorsteinn Thorsteinnsson, personal communication, Feb. 2015). We use densities of 0.9 g cm^{-3} as published in refs 55,58.

Tremor simulation. Tremor was simulated as a superposition of 'rapidly' repeating 'small' earthquakes. The timing and amplitude of these events were represented using comb-like functions. We derived a spike spacing of 4 s in the comb from harmonic frequency bands at a spacing of 0.25 Hz in the real tremor. We tested combs with various amplitude distributions and time spacing variations ranging from 2.5 to 20%. We show a perfectly regular comb, and a comb with a time spacing variation of $\pm 7\%$ and an amplitude distribution that follows the amplitude distribution of the real tremor. For the latter, histograms of the positive amplitudes of the real tremor seismograms were created with 10^{-7} m s^{-1}-wide bins. We simulated tremor and counted the occurrence of each amplitude to demonstrate that we can recover the initially used amplitude distribution. The latter comb fits the real tremor best.

We then convolved the synthetic seismograms generated for a source location beneath cauldron C2 and a 1 Hz Ricker wavelet source time function at all UR station locations with a comb function to simulate one-hour-long tremors. We repeated this for events at seven different depths and for different combs. The resulting tremor was then processed like the real tremor. The observed

seismograms/amplitude spectrograms are shown in Supplementary Fig. 4 for a perfectly regular comb. Figure 4 shows a comb with a time spacing variation of $\pm7\%$ and an amplitude distribution that follows an amplitude distribution as observed in reality.

Numerical modelling of magma flow. The possibility of tremor being generated by magma flow was investigated using the nonlinear excitation of a conduit by the fluid-flow model of Julian[4]. Here, a third-order system of nonlinear equations drives flow through a conduit which induces the surrounding wall oscillations feeding back into the flow via pressure. The model exhibits both stable flow where no tremor is generated and unstable flow which can excite continuous tremor. The model requires several input parameters which determine the frequency of tremor and whether the system is in the stable or unstable regime. A set of parameters constrained from field measurements were input into this model, see Supplementary Table 2. Since the field measurements are highly variable, for each parameter, a lower, intermediate and upper bound value were chosen and the model was run using every possible combination of these parameters. Based on our velocity model we derived a rock density at 3–8 km depth of 2.64–2.79 g cm^{-3}. P wave velocities are 5,288–6,591 m s^{-1} and S wave velocities are 3,011–3,700 m s^{-1}.

For most combinations, the system exhibits steady state behaviour and no tremor is generated. For examples where tremor is generated, the frequency is less than 0.005 Hz—almost two orders of magnitude less than frequencies observed in our field data. Therefore, with these parameters constrained from field measurements, it is highly unlikely that the system will generate tremor with a frequency greater than 0.5 Hz. This result is consistent with other studies where it has been shown that these flow models for high-viscosity, low-flow-rate fluids tend to be in the steady state regime[5,6,23].

Code availability. The array processing was performed using the freely available Python toolbox ObsPy[39,40]. Numerical full wavefield elastic simulations were carried out in SPECFEM3D[46]. A selection of other codes are available through the corresponding author.

Data availability. The seismic data that support the findings of this study are available via the website: 'http://futurevolc.vedur.is'.

References

33. Schmidt, R. O. Multiple emitter location and signal parameter estimation. *IEEE Trans. Antennas Propag.* **AP-34,** 276–280 (1986).
34. Goldstein, P. & Archuleta, R. J. Array analysis of seismic signals. *Geophys. Res. Lett.* **14,** 13–16 (1987).
35. Frankel, A., Hough, S., Friberg, P. & Busby, R. Observations of Loma Prieta aftershocks from a dense array in Sunnyvale, California. *Bull. Seismol. Soc. Am.* **81,** 1900–1922 (1991).
36. Del Pezzo, E., La Rocca, M. & Ibanez, J. Observations of high-frequency scattered waves using dense arrays at Teide volcano. *Bull. Seismol. Soc. Am.* **87,** 1637–1647 (1997).
37. Saccorotti, G. & Del Pezzo, E. A probabilistic approach to the inversion of data from a seismic array and its application to volcanic signals. *Geophys. J. Int.* **143,** 249–261 (2000).
38. Rost, S. & Thomas, C. Array seismology: methods and applications. *Rev. Geophys.* **40,** RG000100 (2002).
39. Beyreuther, M. *et al*. ObsPy: a python toolbox for seismology. *Seismol. Res. Lett.* **81,** 530–533 (2010).
40. Megies, T., Beyreuther, M., Barsch, R., Krischer, L. & Wassermann, J. ObsPy—what can it do for data centers and observatories? *Ann. Geophys.* **54,** 47–58 (2011).
41. La Rocca, M. *et al*. Testing small-aperture array analysis on well-located earthquakes, and application to the location of deep tremor. *Bull. Seismol. Soc. Am.* **98,** 620–635 (2008).
42. Almendros, J. *et al*. A double seismic antenna experiment at Teide volcano: existence of local seismicity and lack of evidences of volcanic tremor. *J. Volcanol. Geotherm. Res.* **103,** 439–462 (2000).
43. Kumagai, H. *et al*. Broadband seismic monitoring of active volcanoes using deterministic and stochastic approaches. *J. Geophys. Res.* **115,** 2156–2202 (2010).
44. Battaglia, J. & Aki, K. Location of seismic events and eruptive fissures on the Piton de la Fournaise volcano using seismic amplitudes. *J. Geophys. Res.* **108,** 2364 (2003).
45. Björnsson, H. Surface and bedrock topography of ice caps in Iceland, mapped by radio echo-sounding. *Ann. Glaciol.* **8,** 11–18 (1986).
46. Tromp, J., Komatitsch, D. & Liu, Q. Spectral-element and adjoint methods in seismology. *Commun. Comput. Phys.* **3,** 1–32 (2008).
47. Martens, H. R. *et al*. Dense seismic network provides new insight into the 2007 Upptyppingar dyke intrusion. *Jökull* **60,** 47–66 (2010).
48. Mitchell, M. A., White, R. S., Roecker, S. & Greenfield, T. Tomographic image of melt storage beneath Askja Volcano, Iceland using local microseismicity. *Geophys. Res. Lett.* **40,** 5040–5046 (2013).
49. Menke, W., West, M., Brandsdóttir, B. & Sparks, D. Compressional and shear velocity structure of the lithosphere in Northern Iceland. *Bull. Seismol. Soc. Am.* **88,** 1561–1571 (1998).
50. Pálmason, G. Seismic refraction investigation of the basalt lavas in northern and eastern Iceland. *Jökull* **13,** 40–60 (1963).
51. Darbyshire, F. A., Bjarnason, I. T., White, R. S. & Flóvenz, Ó. G. Crustal structure above the Iceland mantle plume imaged by the ICEMELT refraction profile. *Geophys. J. Int.* **135,** 1131–1149 (1998).
52. Gardner, G., Gardner, L. W. & Gregory, A. R. Formation velocity and density—the diagnostic basics for statigraphic traps. *Geophysics* **39,** 770–780 (1974).
53. Kohnen, H. The temperature dependence of seismic waves in ice. *J. Glaciol.* **13,** 144–147 (1974).
54. Bentley, C. R. Seismic-wave velocities in anisotropic ice: a comparison of measured and calculated values in and around the deep drill hole at Byrd Station, Antarctica. *J. Geophys. Res.* **77,** 4406–4420 (1972).
55. Dewart, G. *Seismic Investigation of Ice Properties and Bedrock Topography at the Confluence of Two Glaciers, Kaskawulsh Glacier, Yukon Territory, Canada*. Technical Report, Institute of Polar Studies Report No. 27 (Institute of Polar Studies, The Ohio State University, 1968).
56. Alfaro, R., Brandsdóttir, B., Rowlands, D. P., White, R. S. & Gudmundsson, M. T. Structure of the Grímsvötn central volcano under the Vatnajökull icecap, Iceland. *Geophys. J. Int.* **168,** 863–876 (2007).
57. Guðmundsson, M. T. The Grímsvötn caldera, Vatnajökull: subglacial topography and structure of caldera infill. *Jökull* **39,** 1–20 (1989).
58. Kohnen, H. & Gow, A. J. Ultrasonic velocity investigations of crystal anisotropy in deep ice cores from Antarctica. *J. Geophys. Res.* **84,** 4865–4874 (1979).